

High-Resolution Trench Photomosaics from Image-Based Modeling: Workflow and Error Analysis

by Nadine G. Reitman, Scott E. K. Bennett,* Ryan D. Gold,
Richard W. Briggs, and Christopher B. DuRoss

Abstract Photomosaics are commonly used to construct maps of paleoseismic trench exposures, but the conventional process of manually using image-editing software is time consuming and produces undesirable artifacts and distortions. Herein, we document and evaluate the application of image-based modeling (IBM) for creating photomosaics and 3D models of paleoseismic trench exposures, illustrated with a case-study trench across the Wasatch fault in Alpine, Utah. Our results include a structure-from-motion workflow for the semiautomated creation of seamless, high-resolution photomosaics designed for rapid implementation in a field setting. Compared with conventional manual methods, the IBM photomosaic method provides a more accurate, continuous, and detailed record of paleoseismic trench exposures in approximately half the processing time and 15%–20% of the user input time. Our error analysis quantifies the effect of the number and spatial distribution of control points on model accuracy. For this case study, an $\sim 87 \text{ m}^2$ exposure of a benched trench photographed at viewing distances of 1.5–7 m yields a model with $< 2 \text{ cm}$ root mean square error (rmse) with as few as six control points. Rmse decreases as more control points are implemented, but the gains in accuracy are minimal beyond 12 control points. Spreading control points throughout the target area helps to minimize error. We propose that 3D digital models and corresponding photomosaics should be standard practice in paleoseismic exposure archiving. The error analysis serves as a guide for future investigations that seek balance between speed and accuracy during photomosaic and 3D model construction.

Online Material: Image-based modeling workflow for paleoseismic trench photomosaics, 3D trench model, example photomosaic log, table of error analysis data, and Python script for exporting photomosaics in a vertical plane.

Introduction

Active fault studies for seismic-hazard analysis typically yield information on the timing, displacement, rupture extent, and magnitude of past large earthquakes (e.g., [Personius et al., 2007](#); [McCalpin, 2009](#); [Scharer et al., 2014](#)). Such studies commonly include detailed surface maps for site characterization and subsurface trench investigations to assess earthquake histories. Surface maps greatly benefit from high-resolution ($\leq 1 \text{ m}$) topographic data (Fig. 1a), whereas maps (or logs) of geologic relationships exposed in trench walls (Figs. 1b–c and 2a) benefit from detailed ($\leq 1 \text{ cm}$ resolution) basemaps composed of overlapping photos (Figs. 2b and 3a). Stratigraphic and structural contacts between sub-

surface strata exposed in trenches are typically drafted directly onto a composite image of trench-wall photographs (photomosaic) manually constructed using image-editing software (conventional photomosaic) (Fig. 3a). However, conventional photomosaics are time consuming to create, and abrupt changes in contrast and tone at seams between photographs limit their quality and usability. Furthermore, conventional photomosaics do not record the 3D character of the trench exposures. Here, we address these deficiencies with a semiautomated workflow for creating high-resolution photomosaics using structure-from-motion (SFM) image-based modeling (IBM). This method produces accurate, seamless photomosaics and 3D models in a fraction of the time required to produce mosaics with conventional image-editing software.

*Now at U.S. Geological Survey, Department of Earth and Space Sciences, University of Washington, Box 351310, Seattle, Washington 98195.

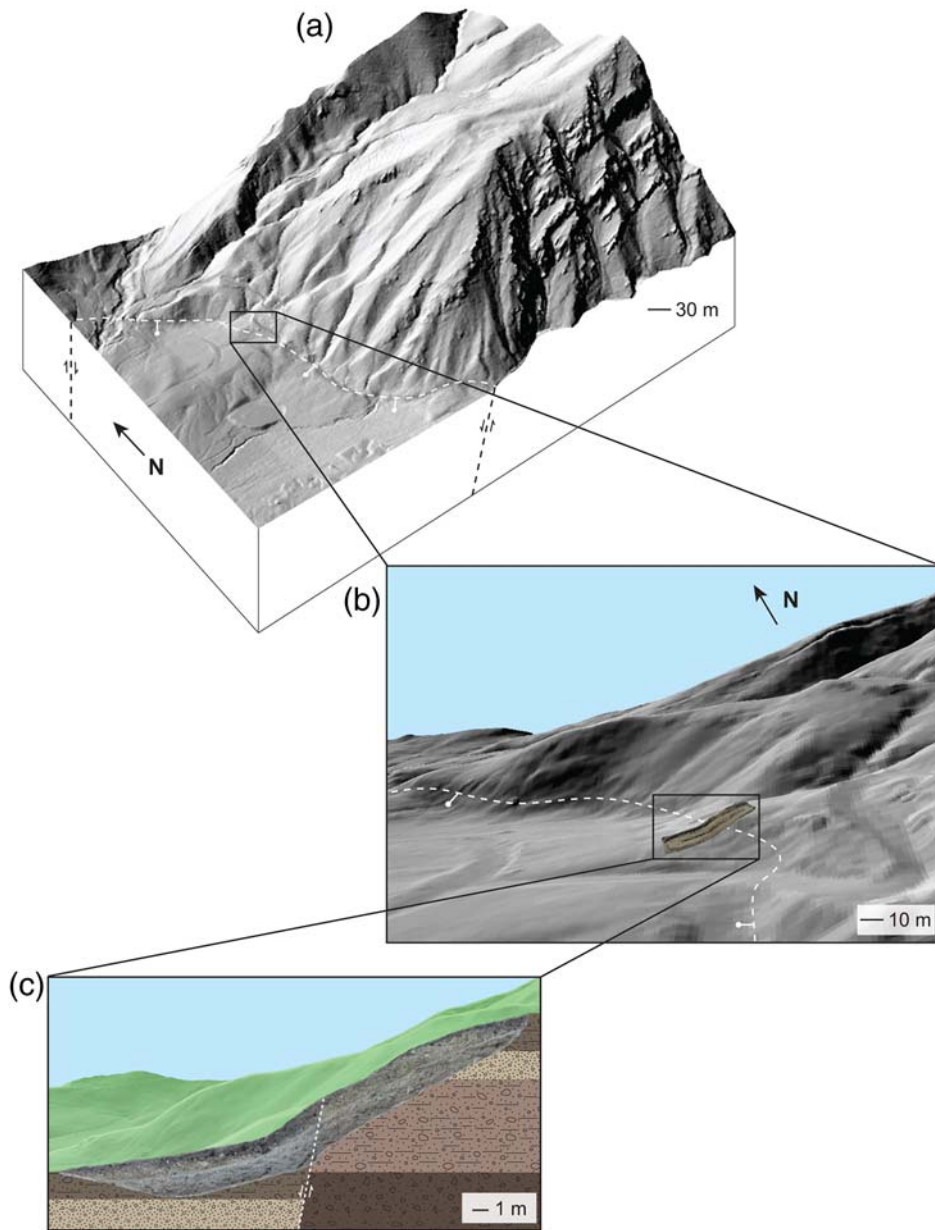


Figure 1. Typical setting of a paleoseismic trench investigation of a normal fault (dashed line). (a) Mountain front-scale perspective view, showing surface topography derived from airborne light detection and ranging (lidar) data. (b) Site-scale perspective view with trench excavation (inside box) perpendicular to the fault scarp. (c) Trench-scale schematic view of subsurface stratigraphy and structures exposed in the trench. The land surface is visible behind the trench. The color version of this figure is available only in the electronic edition.

Image-Based Modeling

IBM is the general process of constructing 3D models from collections of 2D photographs (Snavely, Garg, *et al.*, 2008, and references therein). SFM is a form of IBM developed in the computer vision community to reconstruct unknown 3D scene structure, camera positions, and orientations using feature-matching algorithms (Snavely *et al.*, 2006; Snavely, Garg, *et al.*, 2008; Snavely, Seitz, *et al.*, 2008). Hereafter, we use IBM to refer to the general process and SFM to refer specifically to the feature-matching step. SFM is similar to traditional stereoscopic photogrammetry

in that it relies on overlapping images of a still object or scene to reconstruct 3D scene structure. An important difference, however, is that SFM operates on a set of unordered photographs without the need for organized image acquisition, precalibration of the camera, and control points with known locations, as in traditional photogrammetry. Combined with a multiview stereo algorithm to build dense point clouds, IBM is capable of constructing high-resolution (<1 cm) photorealistic 3D models and seamless photomosaics with only a consumer-grade camera and inexpensive or open-source software. New software packages make the

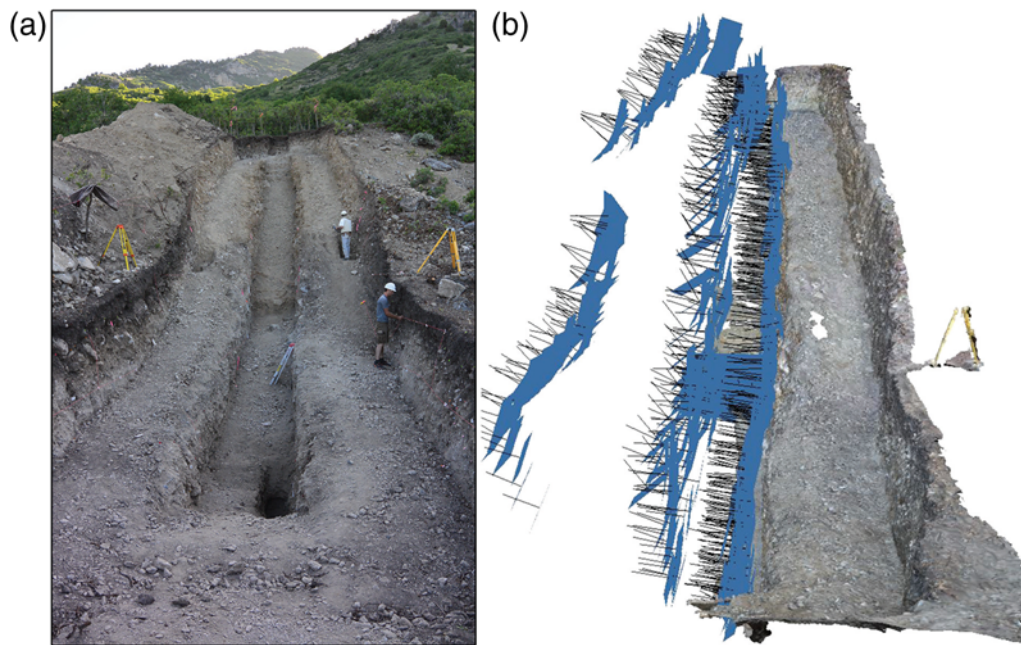


Figure 2. (a) Looking east up the case-study benched trench across the Wasatch fault in Alpine, Utah. (b) Same view of the 3D model of the south wall showing the aligned photographs (rectangles) and their look directions (vectors). Images are approximately orthogonal to the trench walls and acquired from three levels: in the base of the trench, on the opposite bench, and from the ground surface. The tripods are ~1.5 m tall in both panels. The color version of this figure is available only in the electronic edition.

process fast, user-friendly, and automated. See [Bemis *et al.* \(2014\)](#) for examples of commercial and open-source software packages.

IBM applications in the geosciences have recently become widespread and well-documented (e.g., [Harwin and Lucieer, 2012](#); [James and Robson, 2012](#); [Westoby *et al.*, 2012](#); [Fonstad *et al.*, 2013](#); [Lucieer *et al.*, 2013](#); [Bemis *et al.*, 2014](#); [Javernick *et al.*, 2014](#); [Johnson *et al.*, 2014](#); [Kaiser *et al.*, 2014](#); [Tavani *et al.*, 2014](#)). IBM techniques offer a low-cost and portable alternative to airborne and terrestrial light detection and ranging (lidar) surveys to make high-resolution topographic datasets (e.g., [Castillo *et al.*, 2012](#); [James and Robson, 2012](#); [Bemis *et al.*, 2014](#); [Johnson *et al.*, 2014](#)). [Bemis *et al.* \(2013, 2014\)](#) illustrated the potential for using IBM to generate photomosaics and 3D models for complex paleoseismic exposures from pre-existing trench photographs. We build on this prior work by implementing an IBM workflow in a start-to-finish paleoseismic trench study with precise 3D control and rigorous error analysis.

Paleoseismic Trench Investigations

Paleoseismic trench investigations are the primary approach to estimate past earthquake timing, recurrence intervals, per-event displacements, and fault-slip rates for seismic-hazard analysis. Trenches typically expose the fault zone, sedimentary units displaced by faulting, scarp-derived colluvium, and secondary faults and fractures (e.g., [McCalpin, 2009](#)). Detailed mapping of structure and stratigraphy within the trench is essential for reconstructing stratigraphic and geometric relations that are used to infer fault rupture history. In

modern paleoseismic studies, stratigraphic contacts, shear zones, and sample locations are logged directly onto photomosaic basemaps (e.g., [Personius *et al.*, 2007](#)). Required resolution and scale of the photomosaic basemaps depend on the magnitude of the offsets and the grain size of the substrate material. A trench that exposes centimeter- to decimeter-scale displacements of fine-grained deposits (e.g., [Scharer *et al.*, 2014](#)) will require higher resolution and finer-scale basemaps than a trench that exposes decimeter- to meter-scale displacements in coarse material (e.g., [Personius *et al.*, 2007](#)).

Conventional trench-wall photomosaics (Fig. 3a) are created manually and require a string grid overlain on the trench walls, careful image acquisition, and several hours of labor-intensive image manipulation. In the conventional workflow, images are acquired systematically such that each photograph spans one grid rectangle and is shot orthogonal to the trench wall to minimize geometric distortion. Each image is then cropped, color-balanced, and warped in image-editing software and compiled into a composite image of the trench wall.

The primary drawbacks to the conventional photomosaic method are the time required to acquire and edit individual photographs and the poor visual and color continuity of the final photomosaic ([Haddad *et al.*, 2012](#); [Bemis *et al.*, 2014](#)). For example, compiling a photomosaic for an ~250 m² benched trench exposure on the Wasatch fault ([Bennett *et al.*, 2014](#)) took >50 hrs of user input. Frequently observed problems with the conventional approach include distortion at the margins of individual images and parallax exaggerated by 3D irregularities of trench walls (e.g., holes, protruding

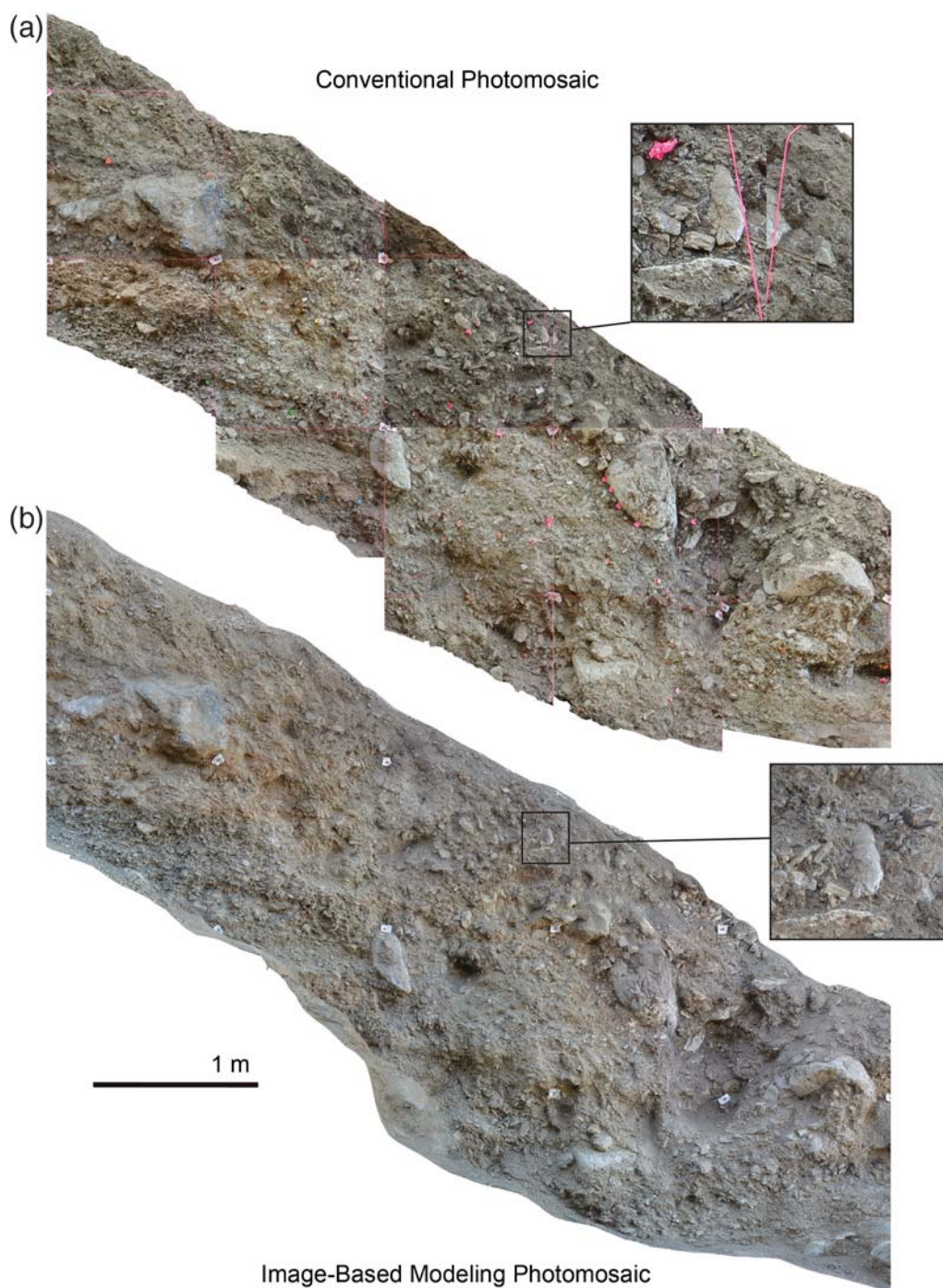


Figure 3. Comparison of photomosaics of the Wasatch fault zone exposed in the lower south wall of the Alpine trench. Images generated using (a) conventional photomosaic methodology via manual processing and tiling of individual images in image-editing software (Adobe Photoshop) and (b) image-based modeling (IBM) methodology using automated software (Agisoft PhotoScan, see [Data and Resources](#)). The duplicated clast highlighted in (a) inset box is represented accurately as a single clast in (b) inset box. Images in (a) acquired 4 June 2014 and (b) 26 May 2014. The color version of this figure is available only in the electronic edition.

clasts; Fig. 3a, inset box). These issues result in misalignment or duplication of features, such as large clasts, and obvious distortion of string grids. Finally, the difficulties inherent in manually color-balancing and aligning images result in photomosaics with obvious seams and poor color continuity (Fig. 3a).

Recently, terrestrial laser scanning (TLS) has been used as an alternative to conventional photomosaics for producing high-resolution 3D georeferenced models of trenches and outcrops (Haddad *et al.*, 2012; Minisini *et al.*, 2014). When coupled with an onboard or mounted camera, TLS produces photorealistic trench models that are more detailed and

accurate than conventional photomosaics (Haddad *et al.*, 2012) and require little postprocessing. However, the equipment required for TLS is costly, fragile, bulky, and requires external power, and the technique can be time-consuming to implement in the field (Castillo *et al.*, 2012; James and Robson, 2012). For these reasons, the TLS method can be prohibitively expensive and/or logistically challenging in remote field sites.

In this study, we demonstrate the utility of IBM in paleoseismic trench investigations to rapidly produce high-resolution trench photomosaic basemaps in a semiautomated workflow in a field setting. We evaluate the speed and accuracy of the IBM technique to construct a detailed photomosaic and a photorealistic 3D model of a paleoseismic trench exposure on the Wasatch fault in Alpine, Utah (Bennett *et al.*, 2015). We also explore the relationship between the number and distribution of ground control points and model accuracy.

Image-Based Modeling Methods

Field Data Collection

IBM 3D models and corresponding 2D photomosaics depend on a sufficient number of overlapping images and accurate control points in order to correctly preserve the 3D geometry and location of the target area. Resolution of the photomosaic is a function of camera sensor resolution and the distance between the camera and the target. We found that a consumer-grade camera with a 14 megapixel sensor and photographs taken 1.5–7 m from the trench wall are sufficient to distinguish very coarse sand and larger material on the photomosaic. Images should overlap $\geq 50\%$ – 60% , be taken roughly orthogonal to the target, extend beyond the area of interest (e.g., include the trench floor and the ground surface above the trench), and be captured from multiple vertical and horizontal positions. Incorporating a few photographs taken at oblique angles can reduce systematic error (James and Robson, 2014). Accuracy of the 3D model generally increases with image density; however, at a minimum, each point in the trench exposure should be visible in at least three photographs. It is advisable to take excess photographs, especially if working in an ephemeral setting.

Geometric accuracy of the model and photomosaic depends on incorporating control points in either relative or absolute coordinates. Our process for establishing precise survey control at the trench site has three steps: (1) conduct Real Time Kinematic Global Positioning System (RTK GPS) surveys of one or more tripod locations at the ground surface (Fig. 2a) and a minimum of three control points on the ground surface surrounding the trench site; these points are postprocessed to obtain coordinates in an absolute coordinate system (e.g., World Geodetic System 1984 [WGS 84] horizontal, North American Vertical Datum of 1988 [NAVD88] vertical), if desired; (2) use a total station at the tripod location(s) to set a grid of points (e.g., nails) into

each trench wall in relative coordinates (i.e., horizontal and vertical trench units); and (3) use the total station to record locations and elevations of select trench grid points to be used as control points for the IBM model. Optionally, after step 2, absolute coordinates and elevations obtained from postprocessed GPS data can be applied to the total station location(s) to place the trench model in an absolute coordinate system during step 3. Recording coordinates of many (~ 50) points enables rigorous error analysis, in which some of the points are incorporated into the model as control points and others are used as checkpoints to test model accuracy.

We demonstrate this workflow with a case study of a normal-fault trench across the Wasatch fault in Alpine, Utah. For this 32-m-long, 3-m-deep, benched trench (Fig. 2), we used a Magellan ProMark 500 RTK GPS system and a TOPCON GPT-7503 Pulse total station to establish site survey control and place a 1×1 m grid of nails in the trench walls. Measurement distances between total station and trench-wall control points ranged from 5 to 25 m. The nail heads were marked with a +, and nails were labeled with relative (trench) coordinates (e.g., 19H 5V). Five ground-surface control points and two total station tripod locations were established and recorded in absolute coordinates with the RTK GPS system. After creating the trench-wall nail grid in relative coordinates, the total station was placed in the Universal Transverse Mercator (UTM) coordinate system using its GPS-established location, with corrections obtained from the Online Positioning User Service (OPUS) of the National Geodetic Survey (see Data and Resources). UTM coordinates of trench-wall control points were recorded with the total station by shooting the center of each nail head in “no-prism” mode. In this trench exposure, establishing the grid and recording coordinates of nail heads took two to three scientists approximately eight hours per wall and resulted in > 50 control points on each wall.

Images were acquired using a Nikon AW 1 mirrorless camera with an 11–27.5 mm (30–74 35-mm equivalent) lens, internal GPS, and 14 megapixel resolution sensor. The camera was set to automatic mode, and images were acquired with ample ambient light (no flash), avoiding direct sunlight and shadows. The photographer stood in the base of the trench to photograph the lowest wall and on the bench to photograph the opposite upper wall, in both cases capturing images from different heights while maintaining a roughly orthogonal orientation to the trench wall (Figs. 2b and 4a). Photographs were also taken from the ground surface (Fig. 2b) to capture the top portion of the opposite upper wall and the ground surface. Images were taken from 1.5 to 7 m away, as dictated by trench geometry. Optical zoom was used when > 3 m away. Image acquisition of both walls took less than two hours and resulted in ~ 1300 photographs, with a goal of total and redundant image coverage from multiple angles and distances. [Ⓔ] See the workflow in the electronic supplement to this article for a more detailed description of field methods.

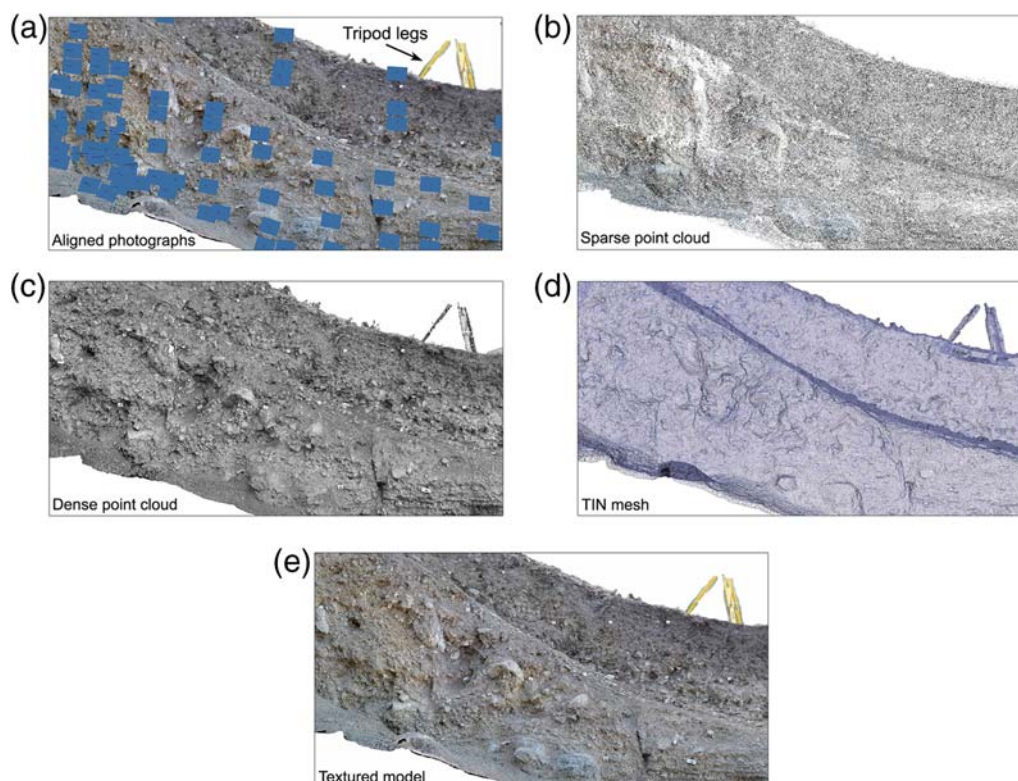


Figure 4. Results of Agisoft PhotoScan processing steps. The tripod legs are ~1.5 m tall. (a) Aligned photographs. The squares represent photographs, and vectors represent their look direction. (b) Sparse point cloud. (c) Dense point cloud. (d) Triangular irregular network (TIN) 3D mesh based on downsampled dense point cloud. (e) Final model with photomosaic derived from automated blending of original photographs draped over the 3D mesh, creating a photorealistic 3D model. The color version of this figure is available only in the electronic edition.

Processing

Automated processing of the trench photographs in IBM software yields a 3D model of the trench exposure. Our processing steps are based on Agisoft PhotoScan Professional Edition v.1.1 (PhotoScan) software (see [Data and Resources](#)). Out-of-focus photographs are discarded prior to processing. No other preprocessing or calibration is required. There are four primary steps (Fig. 4) in the general IBM workflow to transform an uncalibrated, unordered photoset into a 3D photorealistic model: (1) align photos, (2) build dense point cloud, (3) grid point cloud into a 3D surface (mesh), and (4) add color (texture) from original photographs.

Step 1 uses SFM feature-matching algorithms to detect feature points in each photograph, match feature points across photos, and align the photographs. The outputs from step 1 are aligned photographs (camera positions and orientations, Fig. 4a); internal camera-calibration parameters, which include focal lengths and radial and tangential distortion coefficients; and a sparse, colorized point cloud (Fig. 4b).

Step 2 uses a multiview stereo algorithm to make a dense point cloud (Fig. 4c) from the aligned photographs. The dense point cloud comprises millions of points with 3D locations and colors. The dense point cloud is usually two to three orders of magnitude denser than the sparse point cloud.

Step 3 grids the point cloud into a 3D surface or mesh (Fig. 4d). Step 4 uses the original photographs to drape low-

resolution texture (color) over the 3D surface (Fig. 4e), resulting in a photorealistic 3D model. The original photographs can also be mosaicked and exported at high resolution as a 2D photomosaic basemap for trench logging. The resolution of the exported photomosaic depends on the resolution of the input images and can be downsampled during export. See the Agisoft User Manual ([Data and Resources](#)) and [Verhoeven \(2011\)](#) for more information on the specific algorithms employed by PhotoScan.

In practice, the general workflow described above is customized for each project, and control points are required to make geometrically accurate and/or georeferenced models. Adding control points after photograph alignment (step 1) allows the user to take advantage of automated control point placement in IBM software, considerably expediting the process. After control points are entered, the sparse point cloud can be updated to a scaled and/or georeferenced system (linear transformation) and optimized (nonlinear transformation) based on control point coordinates and camera-calibration parameters (output from step 1) to reduce nonlinear warping. To obtain accurate models, it is also important to edit the point cloud to remove points with high error and those beyond the area of interest. ^⑤ See the step-by-step workflow available in the electronic supplement for more details about processing.

The general workflow is altered in one important way to make rapid trench photomosaic basemaps: instead of

building a dense point cloud, we based the 3D model on the sparse point cloud. Creation of the dense point cloud can be omitted when rapid, 2D photomosaic basemaps provide sufficient resolution for trench logging in the field and when 3D surface topography is of secondary importance. We skipped building the dense point cloud because this step is computationally intensive, time-consuming, and does not improve resolution of the exported photomosaic, which depends solely on resolution of the input photographs. Building the dense point cloud may enhance accuracy of the photomosaic, but that greater level of accuracy is often not necessary for trench photomosaics, and the increased processing time should be weighed against the gains in accuracy and project needs. Conversely, if the desired outcome is a high-resolution 3D model of a trench (or high-resolution topography), then building the dense point cloud remains an essential step in the process.

For this case study, the north and south trench walls were processed as separate projects, each covering $\sim 87 \text{ m}^2$ of trench exposure. The south wall model comprises 689 photographs and was optimized with 17 control points. The sparse point cloud has 2.28 million points, with a spatially variable average density of $\sim 200 \text{ points/m}^2$. Pixel resolution of the photomosaic is 0.45 mm, which is more than sufficient to resolve structural and stratigraphic features of interest during trench logging. The north wall model is built from 583 photographs and 15 control points, and the sparse point cloud has 1.98 million points, with an average density of $\sim 125 \text{ points/m}^2$. Resolution of the photomosaic is 0.32 mm. For trench basemaps, the photomosaics were exported at 0.7 mm resolution and overlain with a 1 m^2 grid in a Geographic Information System (GIS). Processing time for one trench wall using PhotoScan v.1.0 on a laptop computer with 16 GB RAM and 2.7 GHz processor was 9 hrs, including ~ 3 hrs of user input. (E) See the electronic supplement to this article for the complete workflow, with a detailed description of the settings used, the time required for each step, a discussion of the photomosaic exporting method, and a script for exporting photomosaics projected onto a vertical plane. We include an example of a 3D, rotatable trench model (E Fig. S1) and an example photomosaic basemap used for logging (E Fig. S2).

Error Analysis

Sources of Error

Accuracy of an IBM model depends on the quality of the photoset; geometry of the target; and number, spatial distribution, and precision of the control points. Here, we evaluate and quantify the accuracy of checkpoints from the SFM sparse point cloud model of the case-study trench in terms of absolute and relative positions. Absolute position, or georeferencing accuracy, is ultimately limited by uncertainty in the RTK GPS survey (measurement error and postprocessing error reported by OPUS), which is $\pm 4.5 \text{ cm}$. We disregard GPS

uncertainty in quantifying internal geometric model accuracy (relative positions), because the GPS survey data are used only to locate the total station in an absolute coordinate system (UTM). In the case-study trench (Fig. 2), control point locations (nail heads) for each wall are recorded without moving the total station, so relative positions are independent of any error in the absolute location of the total station.

Relative accuracy of points in the sparse point cloud is more important than absolute positional accuracy for paleoseismic trench studies and is subject to three sources of error: control point measurement, user error, and error in image alignment and the recovery of camera parameters during the alignment step. Control point measurement was performed with a total station that has a reported measurement accuracy of 1 cm for the distances and settings used in this study (TOPCON, 2007, see [Data and Resources](#)). User error exists at each stage of the process: for example, typical user error occurs during target layout or while sighting the total station on each target (+ on nail heads). User error can be compounded during model construction when the user manually refines control point placement on each photo. We estimate that typical user error in total station sighting and control point placement is $\leq 1 \text{ cm}$, but it may be sporadically higher.

Geometric accuracy is most often affected by errors in image alignment and the recovery of camera parameters. This processing step can cause systematic error that may exceed instrument and user error. Problems with image alignment and camera models can lead to nonlinear deformation in the point cloud, which cannot be corrected during the seven-parameter linear transformation applied during georeferencing (e.g., if using Agisoft, see Agisoft User Manual in [Data and Resources](#)). Nonlinear error due to camera model recovery can be reduced by using camera precalibration to obtain more accurate lens-distortion models (James and Robson, 2014, and references therein). Alternatively, nonlinear error can be minimized by optimizing the sparse point cloud using control points. Because local control points (e.g., nail heads at grid intersections) are usually established as standard practice when mapping paleoseismic trench exposures, we focus on the use of control points for minimizing nonlinear error. At least three control points are required to georeference and scale (linear transform) or optimize (nonlinear transform) the point cloud. It is clear that greater than three control points are required to obtain high internal geometric precision, but it is uncertain how many control points are optimal.

Methods

To assess how many control points are required to obtain maximum internal geometric accuracy for a typical exposure of one trench wall ($\sim 87 \text{ m}^2$), we optimized the sparse point cloud of the Alpine trench south wall in 19 separate models, varying the number and spatial distribution of control points (Fig. 5). We evaluate the results (Fig. 6; E Table S1) by calculating the magnitude of the residual between the observed

and estimated 3D locations of points not used in optimization (checkpoints) using equation (1):

$$\text{Residual}_i = \sqrt{(x_{\text{obs}} - x_{\text{est}})^2 + (y_{\text{obs}} - y_{\text{est}})^2 + (z_{\text{obs}} - z_{\text{est}})^2} \quad (1)$$

Observed, or measured, locations are those recorded with the total station in the field. Estimated locations are those calculated for the checkpoints based on the optimized sparse point cloud. To determine error per model we calculate the mean and median of the residuals for each model (Fig. 6a; ⑤ Table S1). We also calculate the root mean square error (rmse) for each model and for models with the same number of control points (Fig. 6b, ⑤ Table S1), and an error envelope of twice the rmse (shaded region in Fig. 6b). To calculate rmse, we use equation (2):

$$\text{rmse} = \sqrt{\frac{\sum_{i=1}^n (\text{Residual}_i)^2}{n}} \quad (2)$$

We also compared pairs of models (Figs. 5 and 6a; ⑤ Table S1) with 10 (models I and J) and 12 (models K and L) control points distributed throughout the model (scatter style) or around the edges of the model (edges style) to evaluate the effect that spatial distribution of control points has on checkpoint accuracy.

Results

The error analysis (Fig. 6, ⑤ Table S1) indicates that there is a correlation between the number of control points implemented and checkpoint accuracy: using progressively more control points to optimize the sparse point cloud substantially reduces misfit in the model, but the relationship between additional control points and the reduction in error is nonlinear. An exponential fit to the data (Fig. 6a) shows a rapid decay in the mean residuals from three to six control points. This exponential fit represents the average misfit but does not capture the full range of residuals. For example, all models with at least 10 control points scattered throughout the target area have mean residuals < 1 cm (Figs. 5 and 6b; ⑤ Table S1), but the data are not normally distributed (Fig. 6e,f) and maximum residuals can reach 5–7 cm (Fig. 6b).

We use rmse to better understand variation in the data and control point spatial distributions. The rmse analysis (Fig. 6b) indicates rmse values also drop significantly, from ~3 to 1.5 cm, as three to six control points are used. Models with six or more control points have more consistent rmse values of < 2 cm. Although > 95% of all residuals are within an error envelope of twice the rmse (Fig. 6b), each model has 1–2 outliers with larger (up to 9.3 cm) residuals. This may be due to variation in the quality of control point measurement and placement (e.g., user error). The models with > 25 control points were chosen to optimize the point cloud using 50% ($n = 26$ – 27), 75% ($n = 40$), and 100% ($n = 53$) of the 53 available control points, in which the spatial distribution of control points was somewhat randomized. The mod-

els with > 25 control points serve to highlight that some measure of variability in checkpoint accuracy is possible even when using many control points (e.g., the observed increase in rmse for model N; Fig. 6a,b). This variability arises in part from the distribution and quality of the control points used for optimization. Furthermore, because all 53 available control points are used in optimization for model S (Fig. 6a,b), this model represents the practical lowest obtainable limit for checkpoint accuracy in this case study.

Using the minimum number of control points ($n = 3$) for point cloud optimization results in checkpoints that are on average accurate to within 1.5–4 cm (Fig. 6a). Rmse for models with three control points is ~3 cm, but the maximum residuals can be as large as 8 cm (Fig. 6b).

For pairs of models with 10 (I and J) and 12 (K and L) control points, the models with control points scattered throughout the target area yield lower rmse than models with control points near the edges (Figs. 5 and 6a; ⑤ Table S1).

Discussion

Checkpoint Accuracy and Optimal Control Point Distribution

The error analysis evaluates checkpoint accuracy from sparse point clouds optimized with a nonlinear transformation. We draw four primary observations from these results:

1. The use of progressively more control points results in smaller mean residuals and rmse (Fig. 6a,b).
2. Gains in accuracy per added control point are relatively small beyond 12 control points (Fig. 6a,b).
3. Using the minimum number of control points ($n = 3$) yields low mean residuals and rmse (Fig. 6a,b), but results in high scatter (Fig. 6b,c).
4. Higher accuracy is achieved when control points are distributed throughout the target area (Figs. 5 and 6a; ⑤ Table S1).

The error analysis supports the intuitive notion that incorporating more control points results in increasingly accurate model geometries. However, if field time is limited, using only three control points in a typical trench-wall exposure of ~87 m² results in reasonably accurate checkpoints, provided the control points are measured and placed precisely and distributed throughout the target area. We caution that using only a few control points is risky, because the model is more vulnerable to error at individual points, and using additional control points scattered throughout the exposure will increase the likelihood of producing accurate checkpoints. For the target area described in this case study, we find diminishing gains in accuracy for each control point added beyond 12 control points. Although checkpoint accuracy is highest when > 25 control points are used for optimization, the relatively small gains in accuracy should be evaluated against the time spent measuring, recording, and inputting those additional control points.

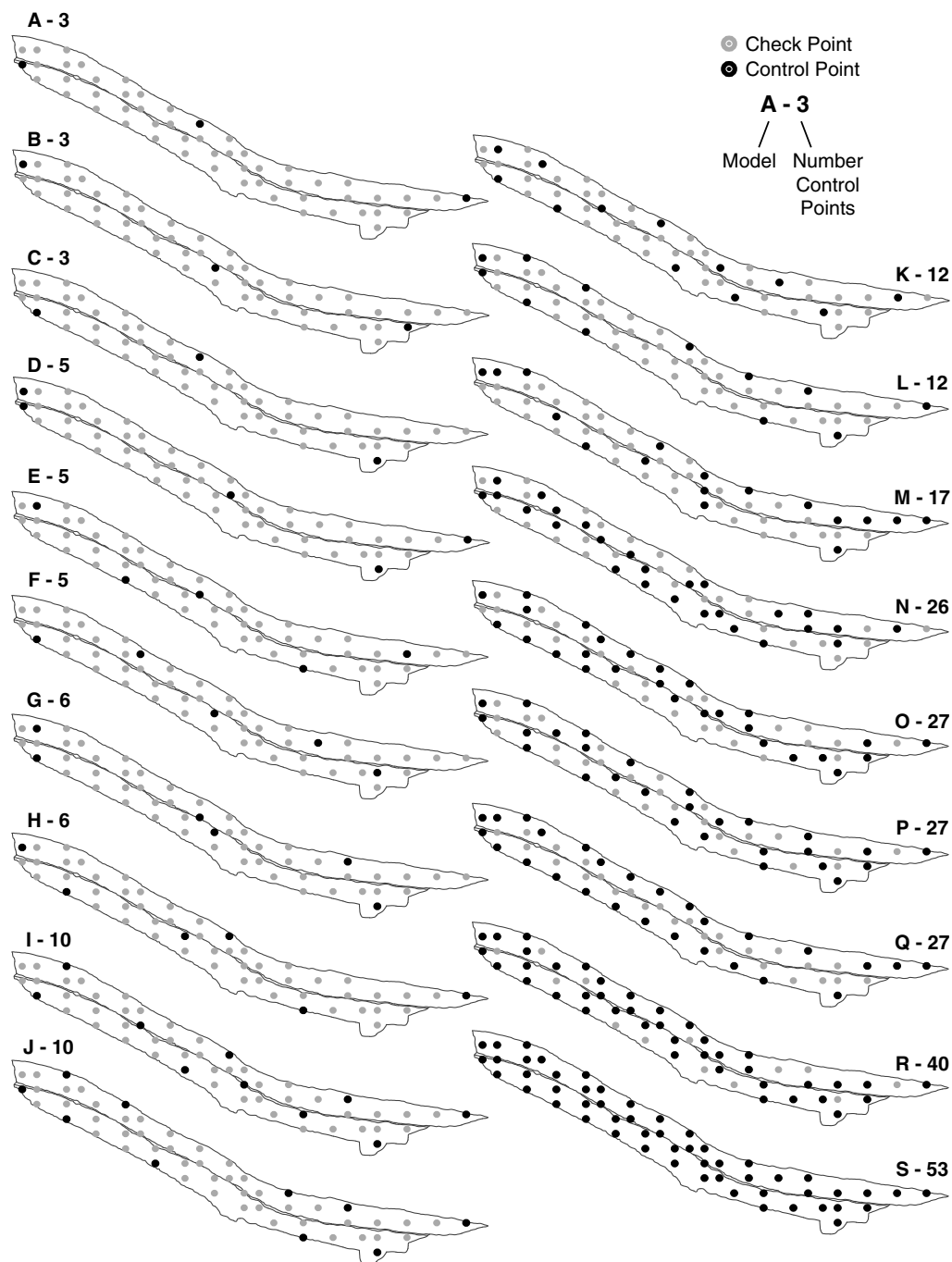


Figure 5. Schematic trench walls illustrating the distribution of control points and checkpoints for each point cloud optimization. Optimal control point distributions have at least 10–12 control points scattered throughout the target area (e.g., models I and K).

We also find that the spatial distribution of control points is an important factor in checkpoint accuracy (Figs. 5 and 6a; ⑤ Table S1). Because models with control points scattered throughout the target area are more accurate than models with control points near the edges, we suggest that scattering control points throughout the target area is a better strategy than placing them only at the edges.

Ultimately the number and distribution of control points implemented depends on the accuracy goals, size, and geometry of the project. For rapid photomosaics of a normal-fault

trench exposure in coarse material with meter-scale offsets, using 3–6 control points per wall ($\sim 87 \text{ m}^2$ exposure) may be sufficient for field logging, but for projects requiring greater accuracy (e.g., trenches in fine-grained deposits with centimeter-scale offsets), at least 12 control points and/or a dense point cloud may be necessary. Similarly, the shape of the target area may affect how many control points are needed. For example, a long, shallow exposure may require twice as many control points as this case study; whereas a square exposure may not require more control points.

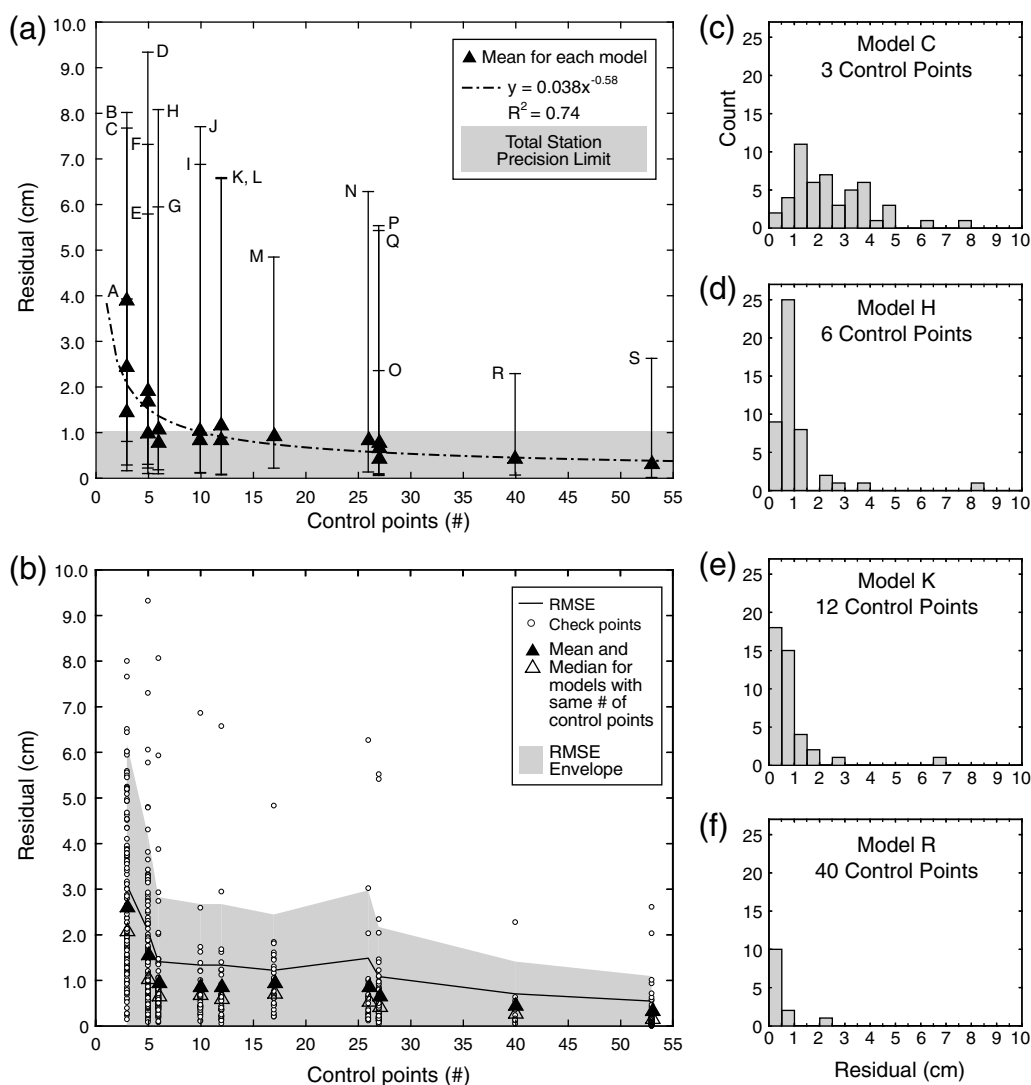


Figure 6. Error analysis. (a) Three-dimensional residuals of checkpoints used in error analysis. Labels A–S indicate models with different quantities and distributions of control points, as illustrated in Figure 5. Control points are scattered throughout the target area for models I and K and at the edges for models J and L. Each model yields an optimized point cloud for which we calculate mean, minimum, and maximum residuals (Table S1). Error bars extend to the maximum and minimum residual for each model. (b) Root mean square error (rmse) analysis. For models with the same number of control points (e.g., models A, B, and C with three control points), the mean and median residuals include points from all models. Checkpoints show the total range in residuals. An error envelope of twice the rmse (shaded area) shows that models having at least six control points are consistently more accurate. For models with the same number of control points arranged in scatter and edges distributions (models I and J with 10 control points and models K and L with 12 control points), the model with the scatter distribution is shown. (c–f) Histograms showing the distribution of checkpoint residuals for four models.

This analysis agrees with [Harwin and Lucieer \(2012\)](#), who found that both the number and distribution of control points impacted the geometric accuracy of checkpoints in a dense point cloud reconstructed from imagery taken with an unmanned aerial vehicle.

Adapting the Workflow for Different Paleoseismic Exposures

The process presented in this case study is meant to serve as a best practices workflow in paleoseismic trench settings in which high accuracy is required, survey equipment

such as an RTK GPS system and a total station are available, and the trench will be open for at least one week. Furthermore, this workflow is primarily designed to facilitate rapid, high-resolution photomosaics using the SFM sparse point cloud. We hope this study serves as a useful guide for future paleoseismic investigations, but it is meant as a jumping-off point rather than a definitive workflow. Here, we discuss ways this workflow can be modified for different paleoseismic exposure settings.

Some of the techniques we use in this bench normal-fault trench may not be optimal for other paleoseismic excavations, as each trench has its own unique geometry and

complexities, along with specific research goals. The resolution and accuracy required for paleoseismic trench photomosaics and 3D models depend on the grain size of the substrate, the stratigraphy, and the magnitude of the offsets. Different trench geometries (e.g., slot, open-pit, benched) (e.g., [McCalpin, 2009](#); [Bemis *et al.*, 2014](#); [Scharer *et al.*, 2014](#)) may require modified photo acquisition and control point deployment strategies. For example, slot trenches will necessitate more photos due to the limited viewing distance, as will any trench requiring ultra-high resolution and accuracy.

The process described in this study utilizes control points with absolute coordinates measured with RTK GPS precision, but this is not required to make scaled trench models and photomosaics (e.g., [Bemis *et al.*, 2014](#)). At a minimum, a 3D scaled model of a trench can be made with only a consumer camera and a tape measure. In this case, distances between at least three pairs of objects in the trench that are visible on the photographs are measured and used to provide model scale, but not absolute position. This approach is suitable for situations in which survey time and resources are extremely limited. [Bemis *et al.* \(2014\)](#) caution that these distance measurements should be taken over the width of the target area, rather than at small intervals. Such long measurements are difficult to capture accurately by hand (e.g., [Castillo *et al.*, 2012](#)), and consequently model errors may be large and unknown.

Additionally, georeferencing may be accomplished using coordinates from GPS-tagged photos, but in this case distance measurements between objects in the trench should be used for optimization because the low-precision GPS in consumer cameras can introduce model error. We used GPS-tagged photos because we found that using a GPS-enabled camera significantly reduced image alignment time in initial testing with PhotoScan v.0.9. However, this benefit is not as pronounced in recent versions of PhotoScan (v.1.1), and poor-quality GPS photos may slightly increase processing time. Error can also arise from the use of handheld GPS devices to measure control points. Users should expect decreased accuracy with any of these methods, as accuracy is influenced by instrument precision limits, user errors, and error in image alignment and camera model recovery. Although high quality, precise survey control data are optimal for research-grade trench studies, we recognize this approach may not be feasible in all field conditions ([Bemis *et al.*, 2014](#)).

One of the benefits of SFM is that the image-matching algorithms can process photographs from multiple views and cameras, enabling rapid photo acquisition and the use of inexpensive cameras. These qualities are desirable in field settings, when quick photo acquisition may be necessary in fleeting good light conditions or an expensive camera could be harmed. For example, trench photos can be acquired simultaneously by multiple people with multiple cameras if field time is extremely limited. However, a number of studies have shown that using a digital single-lens reflex (dSLR) camera with a fixed-focal-length lens and precalibration can significantly reduce error in model geometry (e.g., [James and](#)

[Robson, 2012, 2014](#)). In this case study, we opted not to use a dSLR camera and fixed-focal-length lens because we are able to distinguish very coarse sand on the photomosaics without these tools and because the larger file size increases processing time. Nevertheless, such tools may be needed to obtain adequate accuracy in some trenches.

Advantages of Using IBM for Paleoseismic Photomosaics

The IBM approach for constructing trench photomosaics provides an alternative to the more time-consuming and labor-intensive practice of manually making photomosaics using image-editing software. At the Alpine trench site, a single user acquired photographs just after sunrise, and the photomosaic basemaps were generated and ready for trench logging by the following morning. Photomosaic basemaps for both walls were completed in approximately 18 hrs, though only ~6 of those hours required user input. For comparison, we estimate it would take 3–4 people working 10 hrs each to produce conventional photomosaics for the case-study trench within a day. The IBM methodology used in this study requires only ~15%–20% of the user input time and approximately half of the total processing time that would be required to generate a conventional photomosaic, though exact time saved depends on the size and geometry of the trench, processing settings used, and user familiarity with software. For the case-study trench and photomosaics, user input time was ~2 min/m² of exposure, and total processing time was ~6 min/m² of exposure. We estimate a manual photomosaic takes at least ~12 min/m² of exposure, all requiring user input. Much of the processing time for IBM photomosaics is automated and requires only one user, relieving other members of the field party to tend to tasks at the trench site. The most time-consuming step in creating the photomosaic is inputting control points; however, the accuracy of the final product is highly dependent on survey control, in either a relative or absolute coordinate system. The error analysis presented here (Figs. 5, 6; [Table S1](#)) serves as a guide for future studies in planning control point deployment and finding an optimal balance between speed and accuracy.

Trench photomosaics generated with the IBM method provide basemaps that are more spatially and visually accurate than conventional photomosaics (Fig. 3). Common features in a trench, such as holes, protruding clasts, and benches that are difficult to handle in conventional photomosaics (Fig. 3a), are easily modeled with the IBM approach (Fig. 3b). Furthermore, exported IBM photomosaics are seamless and color-continuous. Although geometrically accurate models can be made using relative coordinates or scale bars, use of an absolute coordinate system (e.g., UTM) allows for a more complete archive of trench data and the 3D model to be displayed and analyzed in the context of detailed site mapping in a GIS environment. Two-dimensional photomosaics of the trench exposure can be placed in a GIS environment and georeferenced with relative coordinates, which facilitates faster digitizing and

subsequent modification of the trench logs, more efficient management of the data, and easier creation of publication-quality trench logs.

IBM also provides an affordable and timesaving alternative to TLS in the documentation of paleoseismic trench exposures. A number of researchers have quantitatively evaluated the accuracy of IBM-derived topographic data compared with laser-based methods such as airborne and terrestrial lidar (Castillo *et al.*, 2012; Harwin and Lucieer, 2012; James and Robson, 2012; Westoby *et al.*, 2012; Fonstad *et al.*, 2013; Johnson *et al.*, 2014). These studies found that IBM products derived from dense point clouds are similar in accuracy and precision to laser-based methods at many scales (James and Robson, 2012) when control points are used for georeferencing (linear transformation) (Harwin and Lucieer, 2012) and optimization (nonlinear transformation) (Johnson *et al.*, 2014). James and Robson (2012) systematically compare IBM dense point clouds with TLS in terms of cost, efficiency, and accuracy at three scales and report that IBM with a dense point cloud is capable of accuracy to 0.1% (i.e., accurate to 1 cm over a project scale of 100 m). On scales ranging from 1 to 1000 m, James and Robson (2012) demonstrate that IBM is more efficient than TLS in terms of field time, cost, and flexibility and produces data of similar quality. Similarly, Castillo *et al.* (2012) calculated that IBM methods are less expensive and faster per meter of exposure than TLS for gully erosion surveys, which are similar in shape and length to paleoseismic trenches. TLS surveying typically requires more field time than IBM, with minimal postprocessing, whereas IBM field data acquisition is faster but must be processed afterwards. However, Castillo *et al.* (2012) found that IBM methods were faster than TLS in both field and processing times in gully erosion surveys. A weakness of the IBM approach is that only surface models can be created, equivalent to first-return digital terrain models generated by lidar methods; however, this is not usually an issue for the fresh exposures studied in paleoseismic trenches, and users can employ automatic point cloud classification and manual editing to remove unwanted points.

Finally, the IBM technique facilitates creation of a 3D digital representation of the trench (© Fig. S1), which may be used to measure fault offsets and the thickness of stratigraphic units, to better visualize reconstructions of progressive deformation, and to convey interpretations more effectively. Detailed 3D models and associated photomosaics provide a way to permanently preserve ephemeral paleoseismic exposures. Although IBM models do not capture the often subtle variations in unit character (e.g., soil texture, hardness, and friability) that paleoseismologists rely on to map trench exposures, they are a substantial improvement on the existing photomosaic basemaps that typically accompany trench studies.

Conclusions

IBM 3D models and 2D photomosaics provide faster, seamless, more accurate, and more detailed records of paleo-

seismic trench investigations than conventional (manual) photomosaic methods. We demonstrate the use of IBM in documenting paleoseismic trench exposures in a case-study trench along the Wasatch fault, compare the IBM and conventional photomosaics constructed for the site, and evaluate geometric accuracy of checkpoints from the SFM sparse point cloud. The method presented here demonstrates that the rapid, semiautomated creation of high-resolution, seamless, georeferenced paleoseismic trench photomosaics can be accomplished approximately twice as fast with ~15%–20% of the user input time as compared with manual photomosaic methods. Checkpoint accuracy increases with the number of control points implemented, and rmse of < 2 cm can be achieved with as few as six control points on a typical benched trench exposure, provided the control points are spatially distributed throughout the target area. We find diminishing gains in accuracy beyond 12 control points. IBM models also provide enhanced visualization, archival, and educational benefits over conventional photomosaics and are a faster, more cost-effective alternative to TLS to make similar products. The methodology, workflow, and error analysis presented here should aid geologists in any tectonic setting in planning and implementing future investigations.

Finally, we advocate that the IBM method, or a similar approach, become standard practice for paleoseismic trench studies. Because of their intrinsically ephemeral nature, paleoseismic trench exposures should be preserved as 3D models with their corresponding high-resolution photomosaics. IBM models and photomosaics provide substantial data preservation with relatively little effort.

Data and Resources

Real Time Kinetic Global Positioning System data were postprocessed using corrections from the National Geodetic Survey's Online Positioning User Service available at <http://www.ngs.noaa.gov/OPUS/> (last accessed May 2014). Model processing was completed using Agisoft PhotoScan Professional Edition v.1.1. The *Agisoft PhotoScan User Manual: Professional Edition*, v.1.1, was downloaded from <http://www.agisoft.com/downloads/user-manuals/> (last accessed January 2015). Useful tips on image capture (How to Get an Image Dataset that Meets PhotoScan Requirements?) are available from http://www.agisoft.com/pdf/tips_and_tricks/Image%20Capture%20Tips%20-%20Equipment%20and%20Shooting%20Scenarios.pdf (last accessed July 2015). The TOPCON Pulse GPT-7500 total station user manual by TOPCON Corporation (2007) was downloaded from http://www.topotopo.dk/uploads/media/manualer/Totalstation/IM_GPT-7500Eng.pdf (last accessed January 2015).

Acknowledgments

Conversations with Edwin Nissen, Kendra Johnson, Adam McKean, and Steve Bowman guided development of the workflow in trench settings. Joshua DeVore and Adam Hiscock provided valuable field assistance. We thank the Agisoft Support Team for providing the export script and

answering technical questions. Reviews by Steve Personius, Mike James, and Sean Bemis significantly improved this manuscript. The U.S. Geological Survey Earthquake Hazards Program supported this work. Any use of trade, product, or firm names is for descriptive purposes only and does not imply endorsement by the U.S. Government.

References

- Bemis, S., S. Micklethwaite, D. Turner, M. R. James, S. Akciz, S. Thiele, and H. A. Bangash (2014). Ground-based and UAV-based photogrammetry: A multi-scale, high resolution mapping tool for structural geology and paleoseismology, *J. Struct. Geol.* **69**, 163–178, doi: [10.1016/j.jsg.2014.10.007](https://doi.org/10.1016/j.jsg.2014.10.007).
- Bemis, S., L. A. Walker, C. Burkett, and J. R. DeVore (2013). Use of 3D models derived from handheld photography in paleoseismology, *Geol. Soc. Am. Abstr. Progr.* **45**, no. 7, 147.
- Bennett, S. E. K., C. B. DuRoss, R. D. Gold, R. W. Briggs, S. F. Personius, and S. A. Mahan (2014). Preliminary paleoseismic trenching results from the Flat Canyon site, southern Provo segment, Wasatch fault zone: Testing Holocene fault-segmentation at the Provo-Nephi segment boundary, *Seismological Society of America Annual Meeting*, Anchorage, Alaska, 30 April–2 May 2014.
- Bennett, S. E. K., C. B. DuRoss, R. D. Gold, R. W. Briggs, S. F. Personius, N. G. Reitman, A. I. Hiscock, J. D. DeVore, H. J. Gray, and S. A. Mahan (2015). History of six surface-faulting Holocene earthquakes at the Alpine trench site, northern Provo segment, Wasatch fault zone, Utah, *Seismological Society of America Annual Meeting*, Pasadena, California, 21–23 April 2015.
- Castillo, C., R. Perez, M. R. James, J. N. Quinton, and J. A. Gomez (2012). Comparing the accuracy of several field methods for measuring gully erosion, *Soil Sci. Soc. Am. J.* **76**, 1319–1332, doi: [10.2136/sssaj2011.0390](https://doi.org/10.2136/sssaj2011.0390).
- Fonstad, M. A., J. T. Dietrich, B. C. Courville, J. L. Jensen, and P. E. Carbonneau (2013). Topographic structure from motion: A new development in photogrammetric measurement, *Earth Surf. Process. Landf.* **38**, 421–430, doi: [10.1002/esp.3366](https://doi.org/10.1002/esp.3366).
- Haddad, D. E., S. O. Akciz, R. A. Arrowsmith, D. D. Rhodes, J. S. Oldow, O. Zielke, N. A. Toke, A. G. Haddad, J. Mauer, and P. Shilpakar (2012). Applications of airborne and terrestrial laser scanning to paleoseismology, *Geosphere* **8**, no. 4, 771–786, doi: [10.1130/GES00701.1](https://doi.org/10.1130/GES00701.1).
- Harwin, S., and A. Lucieer (2012). Assessing the accuracy of georeferenced point clouds produced via multi-view stereopsis from unmanned aerial vehicle (UAV) imagery, *Remote Sens.* **4**, 1573–1599, doi: [10.3390/rs4061573](https://doi.org/10.3390/rs4061573).
- James, M. R., and S. Robson (2012). Straightforward reconstruction of 3D surfaces and topography with a camera: Accuracy and geoscience application, *J. Geophys. Res.* **117**, no. F03017, doi: [10.1029/2011JF002289](https://doi.org/10.1029/2011JF002289).
- James, M. R., and S. Robson (2014). Mitigating systematic error in topographic models derived from UAV and ground-based image networks, *Earth Surf. Process. Landf.* **39**, 1413–1420, doi: [10.1002/esp.3609](https://doi.org/10.1002/esp.3609).
- Javernick, L., J. Brasington, and B. Caruso (2014). Modeling the topography of shallow braided rivers using structure-from-motion photogrammetry, *Geomorphology* **213**, 166–182.
- Johnson, K., E. Nissen, S. Saripalli, J. R. Arrowsmith, P. McGarey, K. Schärer, P. Williams, and K. Blisniuk (2014). Rapid mapping of ultra-fine fault zone topography with structure from motion, *Geosphere* **10**, no. 5, doi: [10.1130/GES01017.1](https://doi.org/10.1130/GES01017.1).
- Kaiser, A., F. Neugirg, G. Rock, C. Muller, F. Haas, J. Ries, and J. Schmidt (2014). Small-scale surface reconstruction and volume calculation of soil erosion in complex Moroccan gully morphology using structure from motion, *Remote Sens.* **6**, no. 8, 7050–7080, doi: [10.3390/rs6087050](https://doi.org/10.3390/rs6087050).
- Lucieer, A., S. M. de Jong, and D. Turner (2013). Mapping landslide displacements using structure from motion (SfM) and image correlation of multi-temporal UAV photography, *Progress Phys. Geogr.* **38**, no. 1, 97–116, doi: [10.1177/0309133313515293](https://doi.org/10.1177/0309133313515293).
- McCalpin, J. P. (Editor) (2009). Paleoseismology, Second Ed., in *International Geophysics Series*, R. Dmowska, D. Hartmann, and H. Thomas Rossby (Series Editors), Vol. 95, Elsevier Academic Press, New York.
- Minisini, D., M. Wang, S. C. Bergman, and C. Aiken (2014). Geological data extraction from lidar 3-D photorealistic models: A case study in an organic-rich mudstone, Eagle Ford Formation, Texas, *Geosphere* **10**, no. 3, 610–626, doi: [10.1130/GES00937.1](https://doi.org/10.1130/GES00937.1).
- Personius, S. F., A. J. Crone, M. N. Machette, D. J. Lidke, L.-A. Bradley, and S. A. Mahan (2007). Logs and scarp data from a paleoseismic investigation of the Surprise Valley fault zone, Modoc County, California, version 1.1, *U.S. Geol. Surv. Scientif. Investigations Map* 2983, 2 sheets.
- Scharer, K., R. Weldon, A. Streig, and T. Fumal (2014). Paleoearthquakes at Frazier Mountain, California delimit extent and frequency of past San Andreas fault ruptures along 1857 trace, *Geophys. Res. Lett.* **41**, no. 13, 4527–4534, doi: [10.1002/2014GL060318](https://doi.org/10.1002/2014GL060318).
- Snaveley, N., R. Garg, S. M. Seitz, and R. Szeliski (2008). Modeling the world from Internet photo collections, *Int. J. Comput. Vis.* **80**, no. 2, 189–210, doi: [10.1007/s11263-007-0107-3](https://doi.org/10.1007/s11263-007-0107-3).
- Snaveley, N., S. M. Seitz, and R. Szeliski (2006). Photo tourism: Exploring photo collections in 3D, *ACM Trans. Graph.* **25**, no. 3, 835–846, doi: [10.1145/1179352.1141964](https://doi.org/10.1145/1179352.1141964).
- Snaveley, N., S. M. Seitz, and R. Szeliski (2008). Finding paths through the world's photos, *ACM Trans. Graph.* **27**, no. 3, 11–21, doi: [10.1145/1360612.1360614](https://doi.org/10.1145/1360612.1360614).
- Tavani, S., P. Granado, A. Corradetti, M. Girundo, A. Iannace, P. Arbués, J. A. Muñoz, and S. Mazzoli (2014). Building a virtual outcrop, extracting geological information from it, and sharing the results in Google Earth via OpenPlot and Photoscan: An example from the Khaviz anticline (Iran), *Comput. Geosci.* **63**, 44–53.
- Verhoeven, G. (2011). Taking computer vision aloft—Archaeological three-dimensional reconstructions from aerial photographs with PhotoScan, *Archaeol. Prospect.* **18**, 67–73, doi: [10.1002/arp.399](https://doi.org/10.1002/arp.399).
- Westoby, M. J., J. Brasington, N. F. Glasser, M. J. Hambrey, and J. M. Reynolds (2012). ‘Structure-from-motion’ photogrammetry: A low-cost, effective tool for geoscience applications, *Geomorphology* **179**, 300–314, doi: [10.1016/j.geomorph.2012.08.021](https://doi.org/10.1016/j.geomorph.2012.08.021).

Geologic Hazards Science Center
U.S. Geological Survey
M.S. 966
PO Box 25046
Denver, Colorado 80225
nreitman@usgs.gov

Manuscript received 4 February 2015;
Published Online 1 September 2015